

AERODYNAMIC PERFORMANCE ANALYSIS OF A NOVEL LIFT-THRUST INTEGRATED ROTARY FLAPPING AERIAL VEHICLE

Jiaqi Liu[1,2,3], Wenqing Yang[1,2,3,*], Yueyang Guo[1,2,3]& Yugang Zhang[1,2,3]

[1]School of Aeronautics, Northwestern Polytechnical University, Xi' an 710072, China

[2]Shenzhen Research Institute of Northwestern Polytechnical University, Shenzhen 518057, China

[3]National Key Laboratory of Aircraft Configuration Design, Xi' an 710072, China

Abstract

Micro aerial vehicles (MAVs) operating under low Reynolds number conditions often suffer from severely constrained aerodynamic performance due to flow separation and viscous effects. Conventional micro flapping-wing vehicles exhibit negative lift during the upstroke phase and insufficient thrust during high-speed forward flight, while micro rotary-wing vehicles face the technical bottleneck of limited aerodynamic efficiency at microscales. To address these challenges, this paper proposes a novel configuration of the lift-thrust integrated rotary flapping aerial vehicle. The core mechanism of this configuration lies in dynamic mode switching within a single cycle: during the first half-cycle, the wing flaps downward in flapping mode to generate most of the required lift and a portion of the thrust; during the second half-cycle, it transitions to active rotation mode to continuously output forward thrust, thereby fundamentally eliminating the negative lift drawback of conventional flapping wings at the fundamental physical level.

Based on the rigid wing assumption, this study systematically investigates the kinematic characteristics and aerodynamic responses of this novel configuration using a high-fidelity unsteady numerical simulation method combining the Navier-Stokes equations and the overset dynamic mesh technique. A kinematic model incorporating both the global inertial and body-fixed coordinate systems is established, and the effects of key kinematic parameters including flapping amplitude, rotation rate, and mode switching phase on the combined lift-thrust characteristics are quantitatively analyzed. The results demonstrate that this lift-thrust integrated design cannot only effectively eliminate the negative lift phenomenon but also significantly improve overall aerodynamic efficiency by optimizing momentum injection through wake vortex structures. This research provides a novel theoretical perspective and quantitative data support for the design of high-efficiency aerodynamic configurations for micro aerial vehicles under low Reynolds number conditions.

Keywords: MAVs(Micro Aerial Vehicles),Numerical Simulation,Aerodynamic Performance,

Low Reynolds Number Conditions,Lift-Thrust Integrated

1. Introduction

Micro Aerial Vehicles (MAVs) outperform conventional fixed-wing aircraft significantly in terms of maneuverability, stealth performance, and other aspects[1]. They have emerged as a frontier research direction with tremendous development potential in the aerospace field. Their application value in cross-domain scenarios such as military reconnaissance and strike, as well as civilian photography and monitoring, has become increasingly prominent, demonstrating broad engineering application prospects[2-4]. In this field, flapping-wing and rotor-wing configurations are two commonly adopted schemes at present. Although both of these two configurations possesses distinct technical characteristics, both struggle to meet the requirements for high-efficiency flight under low Reynolds number conditions, which strictly limits their application depth[5, 6].

The core shortcomings of Micro Flapping-Wing Aerial Vehicles are concentrated in their flight mechanical characteristics: during the wing flapping process, the negative lift phenomenon is prone to occur, resulting in discontinuous lift output that makes it difficult to meet the requirements of high-maneuverability flight; additionally, inertial forces need to be overcome during flapping, leading to additional energy consumption[7]. Micro Rotor-Wing Aerial Vehicles, however, are constrained by low-Reynolds-number aerodynamic characteristics, resulting in relatively low aerodynamic efficiency; meanwhile, their structural design leads to weak load-carrying capacity, making them unable to adapt to complex mission payloads[8-10]. To address these issues, this paper proposes a novel lift-thrust integrated rotary flapping aerial vehicle. By adopting a novel approach of cross-configuration technology integration, a lift-thrust integrated flight mechanism is established, which provides an effective solution for overcoming the limitations of traditional technologies.

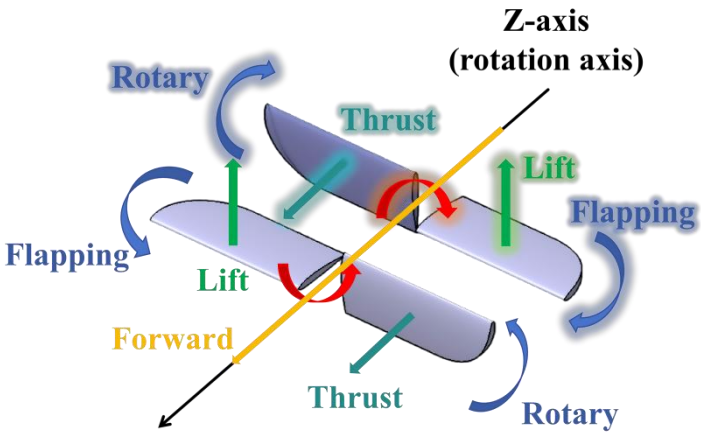


Figure 1 – Basic Mechanism of the Lift-Thrust Integrated Rotary Flapping Aerial Vehicle

Taking active rotation as its core operating mechanism, this configuration achieves the synergistic output of lift and thrust by dynamically switching wing motion modes during the rotational cycle: in the first half-cycle, the wings operate in the flapping mode, efficiently generating the lift required for flight through downward flapping while providing basic forward thrust for the vehicle; in the second half-cycle, the wings switch to the rotational mode, continuously outputting forward thrust via upward rotational motion, thus forming a synergistic working mode of flapping-generated lift and rotation-generated thrust. This design represents a breakthrough in

integrating the lift generation advantages of flapping-wing aircraft and the thrust output characteristics of rotor-wing aircraft. It not only fundamentally eliminates the negative lift phenomenon of traditional flapping-wing configurations and compensates for the thrust shortage during rapid forward flight but also avoids additional inertial power consumption, significantly improving energy utilization efficiency. Consequently, it provides a new technical pathway for high-efficiency flight under low Reynolds number conditions. As shown in Figure 1.

2. Modeling and Method

2.1 Kinematic Modeling

The kinematics of the micro lift-thrust integrated rotary flapping aerial vehicle can be decomposed into the following two fundamental motions. To accurately track the transient compound motion of the wing in three-dimensional space, we establish a multi-reference-frame system based on the standard right-hand rule. As illustrated in Fig. 2, we define a global inertial frame, $o-xyz$, with its origin o fixed at the center of rotation of the vehicle, and its z -axis pointing forward along the longitudinal axis. A body-fixed rotating frame, $o_b-x_by_bz_b$, is subsequently introduced, which co-rotates with the wing around the z -axis at an angular velocity of ω_z . Under the pure rigid-body assumption, the local x_b -axis aligns with the spanwise direction, while the local y_b -axis points vertically upward relative to the body:

a.The wing rotates about the x -axis of the global frame at a constant angular velocity;

b.At specific instances, the wing undergoes a pitching motion about the x_b -axis of the body-fixed frame to execute the transition between the flapping and rotary modes.

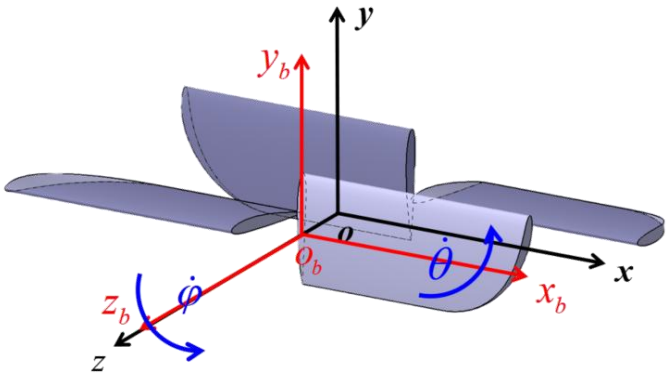


Figure 2 – Coordinate System Definition of the Lift-Thrust Integrated Rotary Flapping Aerial Vehicle

To further develop the kinematic model, we formulate the governing equations of motion for the micro lift-thrust integrated rotary flapping aerial vehicle are formulated as follows:

$$\theta(t)=\frac{\theta_m}{\tanh C_\theta}\tanh\left[C_\theta\sin(2\pi ft)\right] \tag{1}$$

where C_θ serves as a tuning parameter that modulates the smoothness of the pitch angle variation, thereby dictating its rate of change and overall waveform. Specifically, as $C_\theta \to 0$, the function converges to a sinusoidal profile; conversely, as $C_\theta \to \infty$, it asymptotes to a step function. The kinematic profiles corresponding to various C_θ values (0.1, 0.5, 2, 5, and 10) are illustrated in Fig. 3. It is evident that larger values of C_θ yield profiles resembling a square wave, whereas values approaching zero generate near-sinusoidal curves. Furthermore, θ_m denotes the maximum pitch amplitude, and f represents the flapping frequency. For the operational mode of the micro lift-thrust integrated rotary flapping aerial vehicle presented herein, the flapping frequency is strictly synchronized with the rotational frequency, yielding:

$$n = f \tag{2}$$

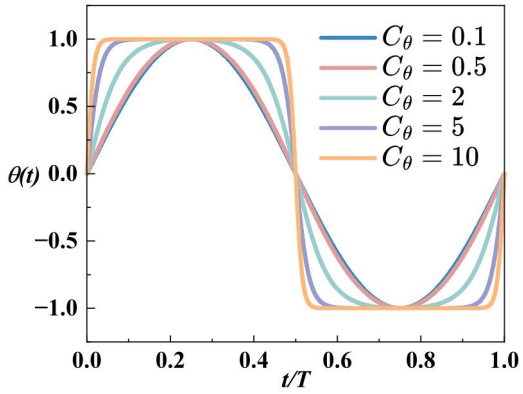


Figure 3 – Image of the Motion Equation for the Lift-Thrust Integrated Rotary Flapping Aerial Vehicle

Defining $\dot{\varphi}$ as the angular velocity of the entire wing rotating about the z-axis of the global frame, and $\dot{\theta}$ as its pitching angular rate about the x_b-axis of the body-fixed frame, the resultant angular velocity of the wing within the global frame is given by:

$$\vec{\omega} = \begin{bmatrix} 0 \\ 0 \\ \dot{\varphi} \end{bmatrix} + \begin{bmatrix} \cos\varphi & -\sin\varphi & 0 \\ \sin\varphi & \cos\varphi & 0 \\ 0 & 0 & 1 \end{bmatrix} \begin{bmatrix} \dot{\theta} \\ 0 \\ 0 \end{bmatrix} \tag{3}$$

where φ denotes the rotation angle of the wing about the z-axis of the global frame:

$$\varphi = 2\pi nt \tag{4}$$

The angular velocity components of the wing about the x-, y-, and z-axes within the global frame are respectively given by:

$$\omega_x = \dot{\theta}\cos\varphi \tag{5}$$

$$\omega_y = \dot{\theta}\sin\varphi \tag{6}$$

$$\omega_z = \dot{\varphi} \tag{7}$$

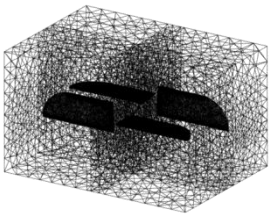
To this end, Equation (1)~(7) fully characterizes all kinematic behaviors of the micro lift-thrust integrated

rotary flapping aerial vehicle. In practical applications, these governing equations may require parameter adjustment to account for specific mechanical conditions. However, as the primary objective of this study is to elucidate the aerodynamic advantages of the micro lift-thrust integrated rotary flapping aerial vehicle, complex structural mechanics effects and large deformations are deliberately excluded from the current scope. Therefore, the presently established kinematic model serves as a robust and sufficient foundation for the subsequent investigations.

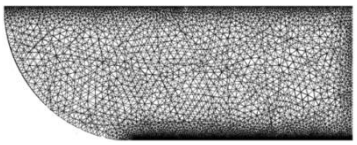
2.2 Mesh Generation

To accurately capture the unsteady flow field characteristics induced by the compound motion of the lift-thrust integrated rotary flapping aerial vehicle, particularly the formation and evolution of the leading-edge vortex (LEV) at low Reynolds numbers, we establish a high-fidelity spatial discretization strategy for the computational domain. Given that the wing undergoes large-amplitude global rotation accompanied by local high-frequency pitching mode transitions, maintaining the robustness and orthogonality of the mesh system is critical to ensuring the convergence of the numerical solver.

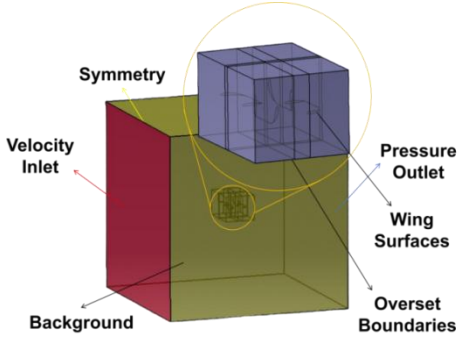
To accurately resolve the intricate physical details within the boundary layer, a dedicated near-wall mesh is deployed over the wing surface. Considering the aerodynamic characteristics at a Reynolds number of $Re \approx 10^5$, the height of the first mesh cell is precisely calculated to satisfy the $y^+ \approx 1$ criterion, thereby guaranteeing full resolution of the viscous sublayer. Furthermore, the surface mesh is substantially refined at the leading and trailing edges to accommodate steep curvature gradients. The mesh expansion ratio is strictly constrained to below 1.15, facilitating a smooth spatial transition into the unstructured tetrahedral mesh in the far field, as depicted in Fig. 4.



(a)Local Flow Field Mesh Model



(b)Simplified Wing Surface's Mesh Model



(c)Schematic of Flow Field Boundaries.

Figure 4 – Computational Model

The fundamental challenge in resolving large-amplitude compound motions lies in the dynamic mesh update strategy. In this study, we employ the overset mesh technique, partitioning the computational domain into a stationary background mesh and a dynamic component mesh that tracks the wing's motion. The distinct advantage of this approach is that, when executing the compound kinematic equations outlined in Section 2.1, the component mesh integrally rotates and pitches as a rigid body alongside the wing. This intrinsically circumvents the critical issue of negative cell volumes caused by severe mesh stretching and compression, a prevalent failure mode in conventional dynamic mesh methods. Furthermore, targeted spatial refinement is meticulously implemented within the volumetric region swept by the wing over a complete cycle. This rigorous resolution strictly prevents the artificial numerical dissipation of shed vortical structures as they convect downstream, which would otherwise occur due to an under-resolved mesh.

2.3 Solver

Given the complex kinematics of the lift-thrust integrated rotary flapping aerial vehicle in a low-Reynolds-number environment, we configure the numerical setup with a pressure-based transient solver, utilizing the absolute velocity formulation to compute the velocity field of the compound motion. For turbulence modeling, the $k-\omega$ Shear Stress Transport (SST) model is selected to accurately resolve the leading-edge vortex and its dynamic evolution during the critical mode transition instants. This model is a prevailing choice for simulating low-Reynolds-number flapping flows, as it effectively balances the high-resolution accuracy of the viscous sublayer in the near-wall region with the computational robustness of the far field.

Regarding the pressure-velocity coupling scheme, we employ the Coupled algorithm. By synchronously solving the momentum and pressure-based continuity equations, the Coupled algorithm significantly enhances numerical stability and accelerates convergence rates when managing intricate compound motions. Spatial discretization for the momentum, turbulent kinetic energy, and specific dissipation rate equations strictly utilizes the second-order upwind scheme. This rigorously limits artificial numerical dissipation, thereby guaranteeing the precision of capturing transient vortical structures.

The physical time step size, Δt, for the unsteady simulation is set to 1/200 of a single motion period, T. This temporal resolution is strategically chosen to ensure the precise capture of transient mechanical features during pitch reversals while pragmatically managing the overall computational cost. Within each time step, the maximum number of iterations is capped at 30. We concurrently monitor the equation residuals alongside the instantaneous lift and thrust coefficients on the wing surface. Convergence is deemed achieved—allowing the simulation to advance to the next operating condition—only when all residual terms drop below 10^{-4} and the aerodynamic monitoring curves exhibit stable, periodic oscillations. The overall computational workflow is illustrated in Fig. 5.

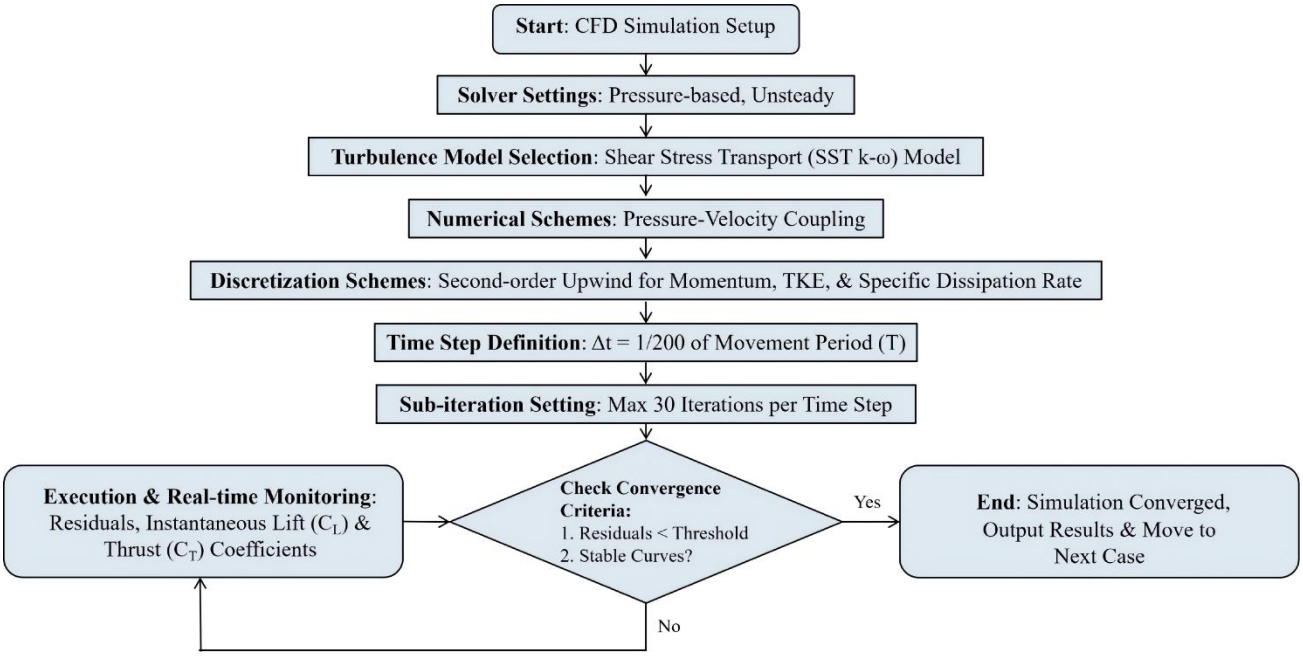


Figure 5 – Flowchart of Unsteady Aerodynamic Numerical Solution

2.4 Validation

To ensure the fidelity and rigor of the three-dimensional unsteady numerical simulations, we systematically performed mesh and time-step independence tests prior to formally investigating the aerodynamic characteristics of the lift-thrust integrated rotary flapping aerial vehicle. Furthermore, the computational accuracy of the numerical solver configured in this study was rigorously validated against the classical water tunnel experiments conducted by Heathcote et al.[11].

The spatial discretization scale fundamentally dictates the resolution of unsteady flow-field details. To preclude mesh-induced artifacts in the calculated unsteady aerodynamic forces, we constructed three sets of unstructured overset mesh systems—coarse, medium, and fine—featuring a constant spatial refinement ratio. As summarized in the table 1, the global cell counts for these three meshes are approximately 3.0 million, 6.0 million, and 9.0 million, respectively. During the spatial refinement process, the first-cell height of the boundary layer, satisfying $y^+ \approx 1$, and the mesh expansion ratio were strictly held constant.

Table 1 – Mesh independence validation plan

Serial \ Object	Number of meshs
1	300W
2	600W
3	900W

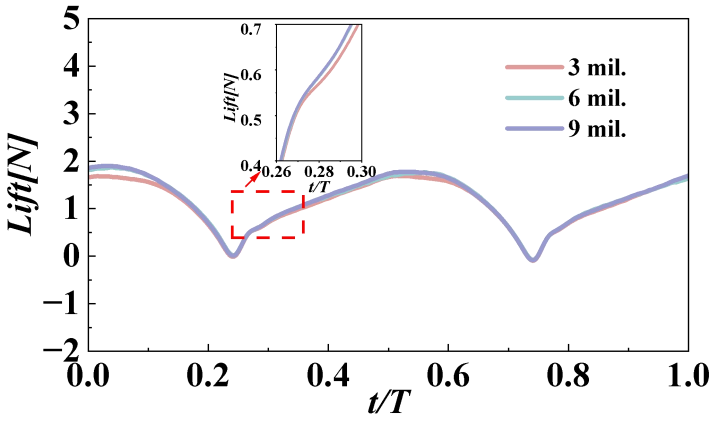


Figure 6 – Lift variation in mesh independence validation

Maintaining strictly identical turbulence modeling, time-step sizes, and boundary conditions, we extracted the transient aerodynamic force profiles over a stable motion cycle under representative operating conditions. As illustrated in Fig. 6, the transient aerodynamic predictions derived from the medium mesh (approximately 6.0 million cells) and the fine mesh (approximately 9.0 million cells) exhibit excellent agreement, with virtually zero phase lag. Although the coarse mesh (approximately 3.0 million cells) demonstrates discernible discrepancies in capturing the peak values relative to the finer meshes, its overall aerodynamic evolution trajectory remains consistent. Weighing the convergence of numerical truncation errors against the substantial computational overhead inherent in three-dimensional unsteady simulations, we ultimately adopted the medium-density mesh system—comprising approximately 6.0 million cells—as the baseline spatial discretization for all subsequent unsteady parametric flow evaluations of the lift-thrust integrated rotary flapping aerial vehicle. This optimal balance guarantees the precise resolution of intricate flow details while effectively averting the superfluous expenditure of computational resources.

With the spatial discretization baseline established, the selection of the physical time step, Δt, fundamentally dictates both the resolution accuracy of high-frequency transient flow structures and the convergence behavior of the implicit solver. To address the highly unsteady aerodynamic characteristics inherent in the lift-thrust integrated rotary flapping aerial vehicle during mode transition instants, we conducted time-step independence tests under a representative operating condition with a rotation/flapping frequency of $f = 5$ Hz. A single, complete physical motion period, T, was uniformly discretized into 100, 200, and 300 steps, corresponding time-step sizes of 0.002 s, 0.001 s, and 0.00067 s, respectively.

Table 2 – Time step independence validation plan

Serial / Object	Number of steps per cycle	Time step
1	100	0.002
2	200	0.001
3	300	0.00067

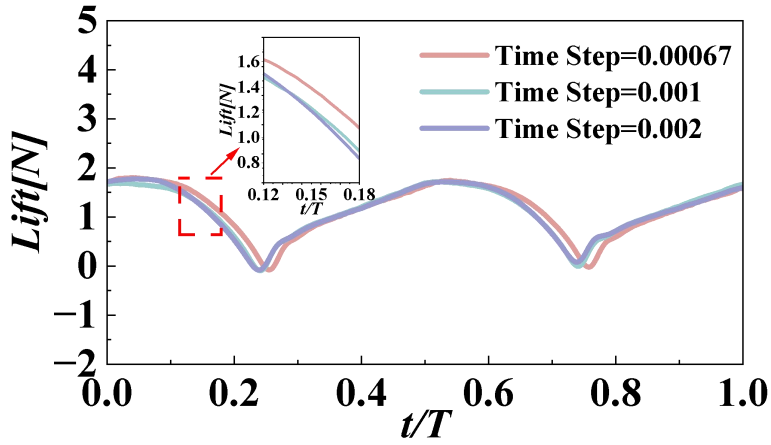


Figure 7 – Lift variation in time step independence validation

For clarity of presentation, the dimensionless time variable t/T is introduced to normalize the kinematic time history of the wing over a single rotation/flapping cycle. As evidenced by the computational results in Fig. 7, discretizing a single period into 100 steps yields a relatively low temporal resolution, which artificially smooths out high-frequency aerodynamic fluctuations and introduces marginal deviations in peak value predictions. Conversely, when the temporal resolution is refined to 200 steps per cycle, the aerodynamic waveforms exhibit exceptional stability and continuity. Further increasing the discretization to 300 steps results in transient lift and thrust profiles that almost perfectly coincide with those obtained using 200 steps. Consequently, this study confirms that a temporal discretization of 200 steps per motion cycle ($\Delta t = 0.001s$) provides robust and sufficient resolution to accurately capture the unsteady aerodynamic characteristics of the lift-thrust integrated rotary flapping aerial vehicle.

To accurately capture the flow-field characteristics of the lift-thrust integrated rotary flapping aerial vehicle undergoing complex kinematics, the numerical solver must be capable of precisely resolving unsteady wing flapping, extensive relative displacements of moving boundaries, and intense three-dimensional effects. To validate the efficacy and accuracy of the proposed numerical framework in addressing these challenges, the classical experimental study conducted by Heathcote[11]was selected as a benchmark for rigorous comparative verification. This landmark experiment systematically investigated the influence of spanwise characteristics on the thrust generation, power input, and propulsive efficiency of rectangular flapping wings. Because the wing in this experiment oscillates in a pure plunging mode, its kinematic boundaries and transient vortex dynamic evolution mechanisms closely resemble those of the downstroke mode of the lift-thrust integrated rotary flapping aerial vehicle, rendering it an ideal reference for validating the unsteady aerodynamic solver. The experiment was conducted in a closed-return, free-surface water tunnel featuring a test section of 381 mm × 508 mm, with the chordwise free-stream velocity strictly maintained at U_∞ = 0.303 m/s. A rigid wing employing the NACA 0012 airfoil profile served as the baseline model for these tests.

For the validation simulations, a three-dimensional overset mesh computational domain was constructed strictly in accordance with the actual physical dimensions and kinematic parameters of the Heathcote experiment[11]. Transient simulations were subsequently executed employing the previously detailed Coupled

pressure-velocity scheme and the $k-\omega$ SST turbulence model. As depicted in the Fig. 8, the unsteady aerodynamic force profiles and mean thrust values derived from our numerical simulations exhibit excellent agreement with the water tunnel measurements, capturing the overall evolutionary trends with high fidelity. Furthermore, the numerical discrepancies across various frequencies are consistently constrained within a minimal margin. This comparative analysis compellingly substantiates that the proposed numerical framework and solver configurations are capable of accurately and reliably simulating the unsteady fluid dynamic behaviors of the lift-thrust integrated rotary flapping aerial vehicle.

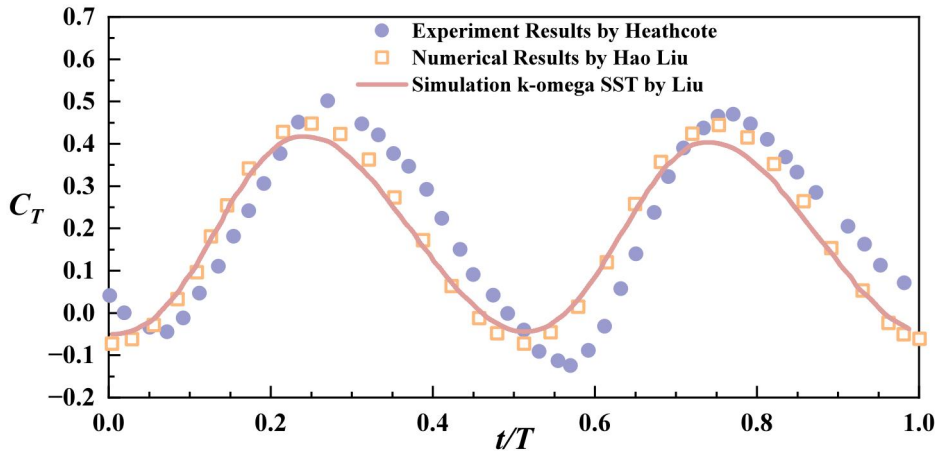


Figure 8 – Comparison for the validation case.

3. Results and Discussion

3.1 Dynamic physical Mechanisms of Unsteady Flow under Typical Conditions

3.1.1 Transient Vortex Topological Evolution Based on Ω-criterion

In low-Reynolds-number unsteady aerodynamics, the pronounced fluctuations in aerodynamic forces are intrinsically linked to the physical mechanisms governing the generation, attachment, evolution, and shedding of separated vortices within the flow field. To elucidate the underlying physical mechanisms of the superior aerodynamic performance of the lift-thrust integrated rotary flapping aerial vehicle from fundamental fluid mechanic principles, we introduce the third-generation vortex identification method—the Ω criterion—to perform high-resolution extractions of the transient vortical structures within the flow field of the lift-thrust integrated rotary flapping aerial vehicle under representative operating conditions. Compared to the conventional Q criterion, the Ω criterion introduces a dimensionless parameter to quantify the ratio of rotational vorticity to the total vorticity. This approach effectively filters out the interference from strong shear flows within the boundary layer, thereby enabling the precise capture of the core topological structures of intense vortices. In light of the "dual-mode" kinematic characteristics exhibited by the lift-thrust integrated rotary flapping aerial vehicle within a single cycle, we separately extracted the three-dimensional transient vortical structures for both the flapping phase and the active rotation phase.

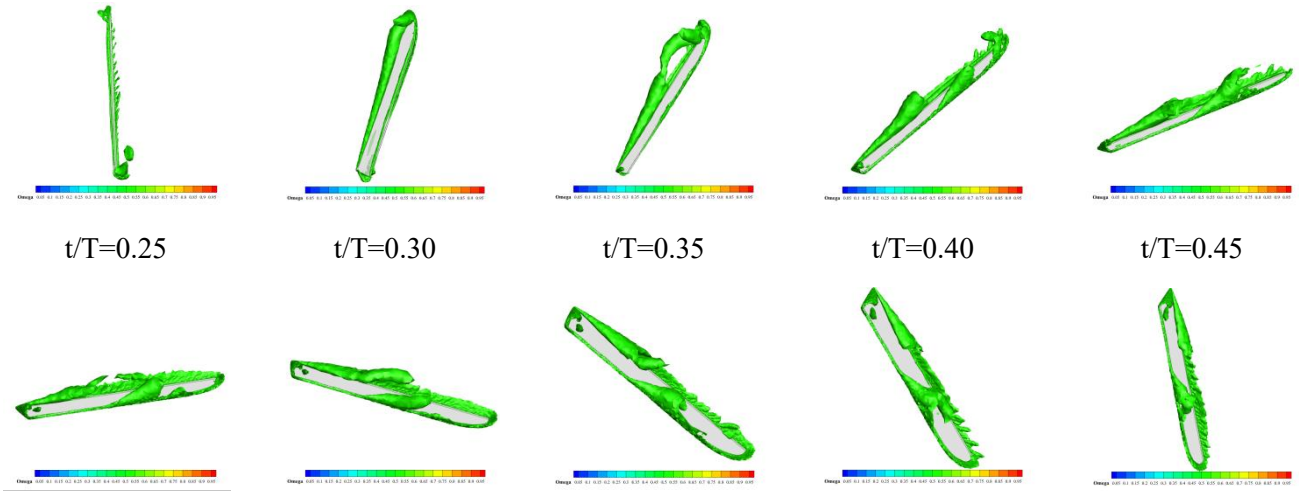


Figure 9 – Results of vortex identification around the wing on one side of the flapping wing during one cycle

During the flapping mode phase, which spans $0.25T \le t \le 0.70T$, the wing executes a downstroke to generate aerodynamic lift. In the initial stage of this phase ($0.25T < t < 0.30T$), the wing has just completed the transition from the rotary mode to the flapping mode. At this instant, fine vortices are uniformly distributed across both sides of the wing surface, while a concentration of high-intensity vortices emerges at the trailing edge of the wing root; concomitantly, the aerodynamic lift reaches its minimum value within the cycle. Subsequently, as the wing continues its downstroke from $0.30T < t < 0.70T$, the leading-edge vortex formed on the upper surface propagates downstream in a spiral trajectory along the spanwise direction. The persistence of this vortical topology effectively prolongs the functional duration of the LEV, thereby generating sustained lift—a classic manifestation of the delayed stall mechanism. Corroborating this with the pressure contours, the low-pressure footprint induced by this flow phenomenon on the upper surface is clearly discernible.

Thereafter, for a conventional flapping-wing configuration or existing rotary-flapping layouts, the wing would typically initiate an upstroke motion. This inversion in the force-acting relationship between the upper and lower surfaces causes the newly oriented lower surface to persistently endure low pressure. Consequently, the lift coefficient drops precipitously—even plunging into negative values—while substantial drag is maintained, rendering it highly detrimental to the aerodynamic efficiency of the vehicle. In stark contrast, for the layout of the proposed lift-thrust integrated rotary flapping aerial vehicle, an examination of the $0.50T < t < 0.70T$ interval reveals the continuous presence of an LEV flowing along the spanwise direction on the upper surface, functioning as a sustained lift generator. Furthermore, beginning at $t = 0.35T$, the formation of highly prominent trailing-edge vortex (TEV) structures can be observed in the aft region of the wing, and the subsequent evolution of this vortex system makes a definitive contribution to thrust generation.

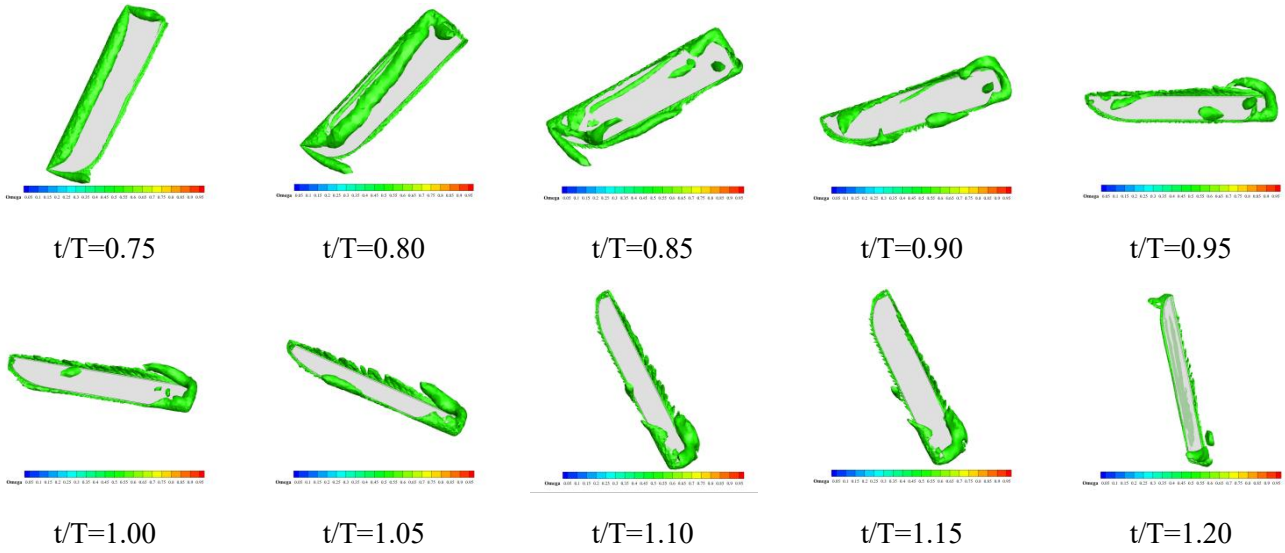


Figure 10 – Results of vortex identification around the wing on one side of the flapping wing during one cycle

The interval spanning from $0.75T$ to $0.20T$ of the subsequent cycle constitutes the rotary mode phase. This phase sequentially follows the cessation of the flapping mode at $t = 0.50T$; together, these two distinct kinematic phases formulate a complete motion cycle of the lift-thrust integrated rotary flapping aerial vehicle. At the onset of this phase ($t = 0.75T$), the wing has just completed its transition from the flapping mode to the rotary mode. At this instant, substantial vortex accumulations are prominent at the leading edge and wingtip, whereas the wing root is populated by densely packed, fine vortices. Subsequently, the wing initiates an upward rotational sweep.

At $t = 0.80T$, the previously generated leading-edge vortex begins to convect chordwise toward the trailing edge. During the interval from $0.85T$ to $1.00T$, vortices continuously shed from the wing surface. Furthermore, compared to the corresponding phase in the flapping mode, the vortical structures here are markedly more chaotic and disorganized. This elevated flow complexity is likely an underlying reason why the temporal evolution of the thrust coefficient is less cleanly defined and periodic than that of the lift coefficient. Throughout the $0.85T < t < 1.20T$ interval, the leading edge, trailing edge, and wingtip are densely lined with fine vortices, whereas high-intensity vortices are generated at the wing root. At $t = 1.20T$, the wing initiates its transition back to the flapping mode, thereby concluding a full operational cycle. The fine vortices shed at the wingtip and the large vortices generated at the root can be morphologically correlated with the vortex distribution surrounding the wing during the $t = 0.25T$ flapping phase.

3.1.2 Spatial Response Characteristics of Surface Pressure

To further elucidate the spatial distribution of aerodynamic forces generated by the lift-thrust integrated rotary flapping aerial vehicle at a fundamental mechanical level, this section extracts the transient surface pressure contours of both the front and hind wings during the flapping and rotary modes under representative operating conditions. A detailed analysis of these spatiotemporal distribution characteristics will reveal the

unique physical advantages of the lift-thrust integrated rotary flapping aerial vehicle in eliminating negative lift and generating substantial thrust.

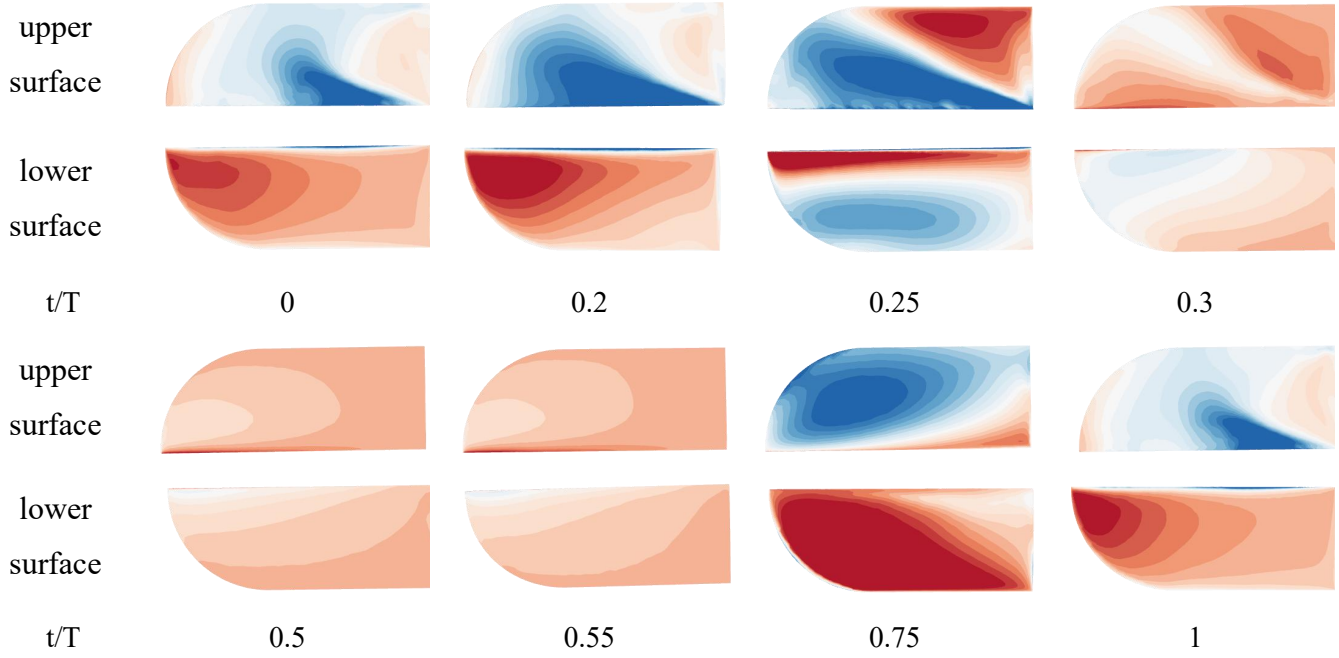


Figure 11 – Pressure contour map of the upper and lower surfaces of the front wing

Fig. 11 illustrates the pressure contours on the upper and lower surfaces of the front wing. During the flapping phase, the upper surface of the front wing exhibits a highly pronounced low-pressure region, culminating in a distinct suction peak near the leading edge. This substantiates the prior observation that the leading-edge vortex remains tightly attached to the upper surface throughout the downstroke, thereby inducing a powerful suction effect that generates the primary aerodynamic lift required for flight. Concurrently, the lower surface of the front wing maintains a relatively high and uniform pressure distribution. This stark pressure differential across the wing ensures a stable transient lift augmentation for the system, even under high-frequency flapping conditions.

Furthermore, the dimensionless time $t/T = 0.25$ marks the kinematic transition from the flapping mode to the rotary mode, whereas $t/T = 0.75$ dictates the transition from the rotary mode back to the flapping mode. As evidenced by the contours, the substantial thrust produced by the lift-thrust integrated rotary flapping aerial vehicle predominantly originates from the rotary-to-flapping mode transition, rather than the flapping-to-rotary transition.

Fig. 12 illustrates the pressure contours on the upper and lower surfaces of the hind wing. A comparative analysis with the front wing reveals a distinct phase-dependent thrust generation mechanism: at $t/T = 0.25$, the thrust is predominantly provided by the hind wing, whereas at $t/T = 0.75$, the thrust is primarily generated by the front wing. Notably, the positive pressure distribution on the lower surface of the hind wing at $t/T = 0.25$ exhibits near-identical spatial characteristics to that on the lower surface of the front wing at $t/T = 0.75$. However, the magnitude of the negative pressure on the upper surface of the hind wing at

$t/T = 0.25$ significantly exceeds that on the upper surface of the front wing at $t/T = 0.75$. This pressure disparity fundamentally elucidates why the thrust peak observed at $t/T = 0.25$ is marginally higher. Furthermore, it concurrently accounts for the emergence of dual thrust peaks within a single kinematic cycle. While the current section unveils the underlying physical origins of this phenomenon, a comprehensive characterization of these transient lift and thrust variations was previously detailed in Section 3.2.1 through the presentation of full-cycle aerodynamic force curves.

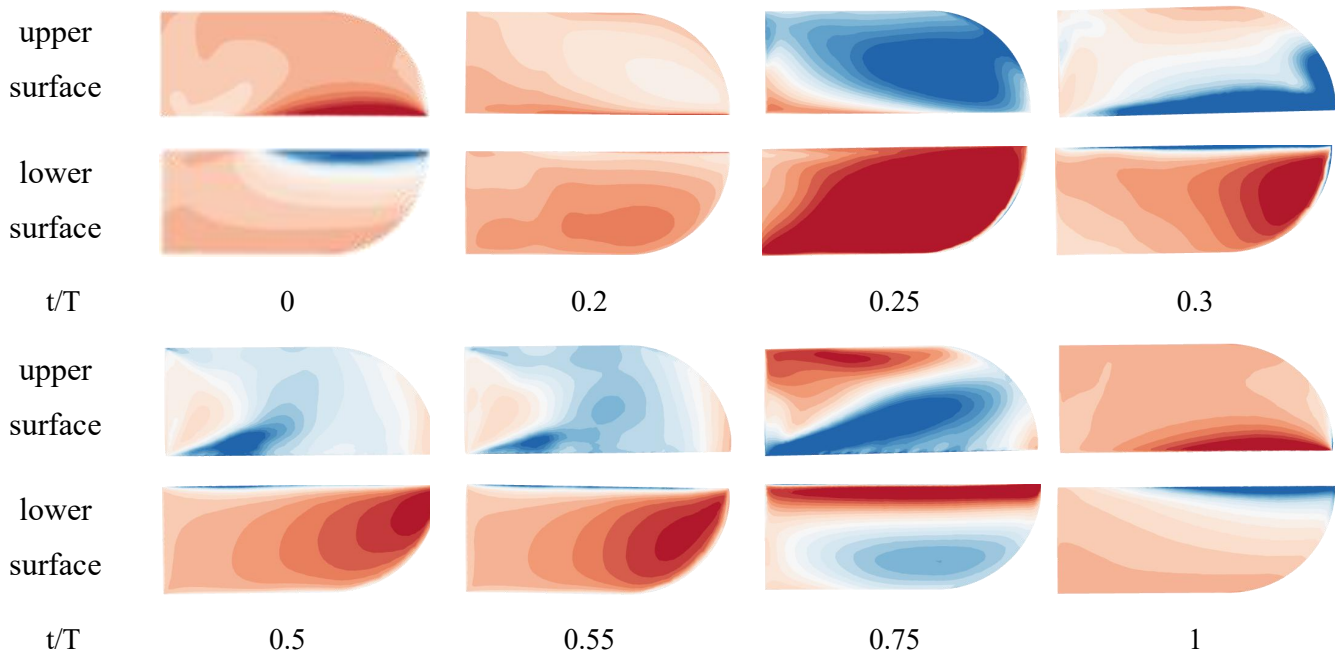


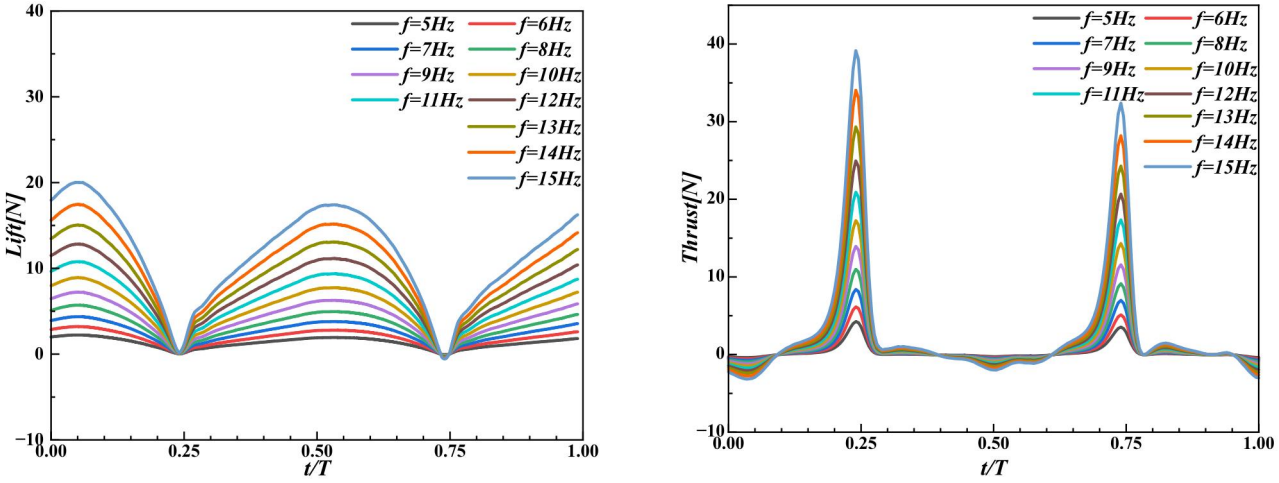
Figure 12 – Pressure contour map of the upper and lower surfaces of the behind wing

3.2 Effects of Kinematic

Having elucidated the unsteady vortex dynamic evolution mechanisms of the lift-thrust integrated rotary flapping aerial vehicle over a single kinematic cycle, this section proceeds to quantitatively investigate how the system's characteristic kinematic frequency and aspect ratio modulate its macroscopic aerodynamic responses.

3.2.1 Frequency

In low-Reynolds-number unsteady flows, the rotation/flapping frequency fundamentally dictates not only the transient kinematic boundaries of the wing but also the energy injection rate into the flow field and the lifespan of separated vortical structures. To systematically evaluate the influence of these frequency effects on aerodynamic performance, we extract the transient lift and thrust histories over a complete physical cycle of the lift-thrust integrated rotary flapping aerial vehicle across various operating frequencies.



(a)Calculation results of the lift

(b)Calculation results of the thrust

Figure 13 – Transient lift and thrust time-history curves of the lift-thrust integrated rotary flapping aerial vehicle over a complete physical cycle

The lift evolution profiles illustrated in Fig. 13(a) indicate that as the rotation/flapping frequency increases, both the transient lift peak and the time-averaged lift coefficient within a single cycle exhibit a pronounced nonlinear growth trend. From an unsteady aerodynamic perspective, this aerodynamic augmentation is primarily driven by the dynamic variation of the effective angle of attack and the vorticity accumulation effect during the first half-cycle (the downstroke mode). The high-frequency downstroke dramatically intensifies the instantaneous downwash velocity at the wing section, causing the actual aerodynamic angle of attack to rapidly surpass the critical static stall threshold. This intense dynamic unsteady effect compels the leading-edge vortex to rapidly roll up and accumulate substantial circulation within an exceptionally brief duration. Concomitant with the frequency increase, the suction effect exerted by the low-pressure core of the LEV on the upper wing surface is exponentially amplified, thereby inducing an exceptionally high transient lift peak during the downstroke phase.

Concurrently, the temporal evolution of thrust depicted in Fig. 13(b) further elucidates the decisive contribution of high-frequency kinematics to thrust generation. During the second half-cycle (the rotary mode), the wing actively rotates to accelerate and expel the surrounding fluid into the wake region. As the rotational frequency increases, both the tangential velocity and the normal acceleration of the wing surface surge synchronously. Consequently, the centrifugal inertial forces within the flow field significantly intensify the radial and chordwise transport of the attached vortical structures. This high-frequency mechanical pumping effect accelerates the breakdown and shedding of large-scale separated vortices, resulting in a substantial surge in the fluid momentum injected into the wake per cycle. The data intuitively demonstrate that under high-frequency operating conditions, the thrust profiles not only achieve an order-of-magnitude leap in their positive peaks but also exhibit a markedly expanded integral area of net thrust, effectively overcoming the pressure drag of the system.

Taken together, elevating the operating frequency serves as a highly effective kinematic control strategy

for enhancing the overall aerodynamic performance of the lift-thrust integrated rotary flapping aerial vehicle. The high-frequency compound kinematics not only amplify the lift augmentation during the downstroke mode by accentuating the delayed stall mechanism, but also propel the thrust output of the rotary mode to new extrema via intense wake momentum exchange. Consequently, these findings establish robust empirical substantiation and a rigorous theoretical foundation for the design of high-maneuverability flight envelopes for this class of micro aerial vehicles operating within low-Reynolds-number environments.

4. Conclusions

In this study, we investigate a novel lift-thrust integrated rotary flapping aerial vehicle, performing high-fidelity numerical simulations of its complex compound kinematics based on a pure rigid-body assumption. Initially, we formulated nonlinear kinematic equations incorporating a smooth transition operator, and precisely resolved the unsteady flow field utilizing the overset mesh technique in conjunction with a Coupled solver. The computational results accurately captured the thrust evolution laws within the unsteady dynamics, corroborating the efficacy of the proposed numerical methodology in handling moving boundaries and highly unsteady flows. Throughout the research, we systematically analyzed the effects of varying rotational frequencies and surface pressure distribution characteristics on aerodynamic performance, and explored the synergistic mechanisms between the front and hind wings. The principal conclusions are as follows:

1.The aerodynamic performance of the lift-thrust integrated rotary flapping aerial vehicle exhibits a significant augmentation effect with increasing kinematic frequency. The high-frequency downstroke actively triggers the delayed stall mechanism by enhancing leading-edge vortex attachment and circulation accumulation, thereby enabling an order-of-magnitude leap in transient lift and thrust peaks.

2.The mode transition mechanism fundamentally eliminates the "negative lift" phenomenon ubiquitously observed during the recovery stroke of conventional flapping wings. Pressure field analysis demonstrates that by substituting the passive upstroke with an active rotary mode, the wing sustains a positive pressure differential throughout the entire cycle, successfully converting intrinsic aerodynamic losses into continuous forward thrust.

3.The front and hind wings exhibit remarkable phase synergy and aerodynamic complementarity during the compound motion. Both wings serve dual functions of lift generation and thrust output; modulated by a phase difference, they respectively contribute the dominant share of lift and thrust at distinct intervals within a single cycle. This temporal load-alternation and compensation mechanism effectively dampens the severe fluctuations of the total transient forces, significantly enhancing the time-averaged aerodynamic efficiency of the vehicle.

In practical applications, the layout of the lift-thrust integrated rotary flapping aerial vehicle offers a novel paradigm for micro aerial vehicles to overcome performance bottlenecks at low Reynolds numbers. By dynamically adjusting the smoothness and phase of the mode transition, the vehicle can optimize the allocation of lift and thrust according to diverse mission requirements. Such precise manipulation of unsteady vortex dynamic characteristics will substantially augment the flight stability and maneuverability of drones in complex, confined spaces.

In subsequent research phases, we will conduct a comprehensive parametric optimization analysis of the lift-thrust integrated rotary flapping aerial vehicle. This analysis will focus on critical factors including the dynamic optimization of the mode transition smoothing factor, the overlap ratio between the front and hind wings, the wing aspect ratio, and the power consumption characteristics under unsteady kinematics. This research aims to provide crucial theoretical support for the design and flight control of future high-efficiency, micro lift-thrust integrated rotary flapping aerial vehicles, thereby propelling the development of next-generation aeronautical technologies at the micro-scale.

5. Contact Author Email Address

Mailto: yangwenqing@nwpu.edu.cn

6. Copyright Statement

The authors confirm that they, and/or their company or organization, hold copyright on all of the original material included in this paper. The authors also confirm that they have obtained permission, from the copyright holder of any third party material included in this paper, to publish it as part of their paper. The authors confirm that they give permission, or have obtained permission from the copyright holder of this paper, for the publication and distribution of this paper as part of the ICAS proceedings or as individual off-prints from the proceedings.

7. Acknowledgements

This study was supported by the National Natural Science Foundation of China (No. 52275293).

8. References

[1] SONG F, YAN Y, SUN J. Review of insect-inspired wing micro air vehicle[J]. Arthropod Structure & Development, 2023,72: 101225.

[2] SINGH S, ZUBER M, HAMIDON M N, et al. Classification of actuation mechanism designs with structural block diagrams for flapping-wing drones: A comprehensive review[J]. Progress in Aerospace Sciences, 2022,132: 100833.

[3] KARÁSEK M, MUIJRES F T, De WAGTER C, et al. A tailless aerial robotic flapper reveals that flies use torque coupling in rapid banked turns[J]. Science, 2018,361(6407): 1089-1094.

[4] PHAN H V, PARK H C. Insect-inspired, tailless, hover-capable flapping-wing robots: Recent progress, challenges, and future directions[J]. Progress in Aerospace Sciences, 2019,111: 100573.

[5] YANG W Q, GUO Y Y, DONG Y B, et al. Research progress on fluid structure interaction of bionic flexible flapping wing UAV[J]. Acta Aeronautica et Astronautica Sinica, 2024, 45(17): 530069 (in Chinese).

[6] SHAHZAD A, TIAN F, YOUNG J, et al. Effects of hawkmoth-like flexibility on the aerodynamic performance of flapping wings with different shapes and aspect ratios[J]. Physics of Fluids, 2018,30(9): 91902.

[7] YANG X, SONG B, YANG W, et al. Study of aerodynamic and inertial forces of a dovelike flapping-wing MAV by combining experimental and numerical methods[J]. Chinese Journal of Aeronautics, 2022,35(6): 63-76.

[8] CHEN L, CHENG C, ZHOU C, et al. Flapping rotary wing: A novel low-Reynolds number layout merging bionic features into micro rotors[J]. Progress in Aerospace Sciences, 2024,146: 100984.

[9] WU J, CHENG C, ZHANG Y, et al. Design of a hover-capable flapping wing micro air vehicle with abdomen-wing coupled control[J]. Chinese Journal of Aeronautics, 2026,39(4): 103807.

[10] HAO J, ZHANG Y, ZHOU C, et al. Aerodynamic performance of hovering micro revolving wings in ground and ceiling effects at low Reynolds number[J]. Chinese Journal of Aeronautics, 2023,36(1): 152-165.

[11] HEATHCOTE S, WANG Z, GURSUL I. Effect of spanwise flexibility on flapping wing propulsion[J]. Journal of Fluids and Structures, 2008,24(2): 183-199.